

# The Shape of Dark Matter Haloes in the Aquarius Simulations: Evolution and Memory

Carlos A. Vera-Ciro<sup>1\*</sup>, Laura V. Sales<sup>1,4</sup>, Amina Helmi<sup>1</sup>, Carlos S. Frenk<sup>2</sup>,  
Julio F. Navarro<sup>3</sup>, Volker Springel<sup>5,6</sup>, Mark Vogelsberger<sup>7</sup> and Simon D. M. White<sup>4</sup>

<sup>1</sup> Kapteyn Astronomical Institute, Univ. of Groningen, P.O. Box 800, 9700 AV Groningen, The Netherlands

<sup>2</sup> Institute for Computational Cosmology, Dep. of Physics, Univ. of Durham, South Road, Durham DH1 3LE, UK

<sup>3</sup> Dep. of Physics & Astron., University of Victoria, Victoria, BC, V8P 5C2, Canada

<sup>4</sup> Max-Planck-Institut für Astrophysik, Karl-Schwarzschild-Straße, 1, 85740 Garching bei München, Germany

<sup>5</sup> Heidelberg Institute for Theoretical Studies, Schloss- Wolfsbrunnenweg 35, 69118 Heidelberg, Germany

<sup>6</sup> Zentrum für Astronomie der Universität Heidelberg, Astronomisches Recheninstitut, Mönchhofstr. 12-14, 69120 Heidelberg, Germany

<sup>7</sup> Harvard-Smithsonian Center for Astrophysics, 60 Garden St., Cambridge, MA 02138, USA

8 April 2011

## ABSTRACT

We use the high resolution cosmological  $N$ -body simulations from the Aquarius project to investigate in detail the mechanisms that determine the shape of Milky Way-type dark matter haloes. We find that, when measured at the instantaneous virial radius, the shape of individual haloes changes with time, evolving from a typically prolate configuration at early stages to a more triaxial/oblate geometry at the present day. This evolution in halo shape correlates well with the distribution of the infalling material: prolate configurations arise when haloes are fed through narrow filaments, which characterizes the early epochs of halo assembly, whereas triaxial/oblate configurations result as the accretion turns more isotropic at later times. Interestingly, at redshift  $z = 0$ , clear imprints of the past history of each halo are recorded in their shapes at different radii, which also exhibit a variation from prolate in the inner regions to triaxial/oblate in the outskirts. Provided that the Aquarius haloes are fair representatives of Milky Way-like  $10^{12}M_{\odot}$  objects, we conclude that the shape of such dark matter haloes is a complex, time-dependent property, with each radial shell retaining memory of the conditions at the time of collapse.

**Key words:** galaxies:haloes, galaxies:formation, galaxies:evolution, cosmology:dark matter

## 1 INTRODUCTION

In our current understanding of the Universe, dark matter haloes constitute an integral part of galaxies. Their properties, especially their density profile and shape, have received significant attention in recent years as they have been argued to be sensitive to the fundamental properties of the dark matter particles. Numerical simulations have been extensively used to study the characteristics of the dark matter haloes, exploring for example the effects of the environment, mass assembly history and the nature of dark matter itself (e.g., Bullock 2002; Bett et al. 2007; Macciò et al. 2007; Hahn et al. 2007; Spergel & Steinhardt 2000; Yoshida et al.

2000; Avila-Reese et al. 2001; Strigari et al. 2007; Wang & White 2009).

The first fully analytical models of the formation of dark matter haloes such as the top-hat spherical collapse model (Gunn & Gott 1972; Fillmore & Goldreich 1984), considered highly symmetric configurations. However, the pioneering work of Frenk et al. (1988); Dubinski & Carlberg (1991); Warren et al. (1992); Cole & Lacey (1996); Thomas et al. (1998) demonstrated important deviations from spherical symmetry by measuring the shape of dark matter haloes in numerical  $N$ -body simulations evolved in a fully cosmological context. These authors consistently found that after virialization, dark matter haloes are triaxial with more prolate shapes towards the centre and more oblate shapes in the outskirts. Recent high resolution  $N$ -body simulations

\* E-mail: cavera@astro.rug.nl

have yielded similar conclusions (Jing & Suto 2002; Bailin & Steinmetz 2005; Kasun & Evrard 2005; Hopkins et al. 2005; Bett et al. 2007; Hayashi et al. 2007; Kuhlen et al. 2007; Stadel et al. 2009; Diemand & Moore 2011).

Further studies based on numerical simulations have also revealed that the environment and mass assembly history of a halo may play a crucial role in determining its shape. Pioneering work by Tormen (1997) and Colberg et al. (1999) suggested that the anisotropic infall of matter onto cluster-sized haloes was largely responsible for their shape, orientations and dynamics at different times. Because infall is governed by the surrounding large scale structure, we expect significant correlations between the halo shapes and their environment, although evidence both against and in support of such trends have been reported so far in the literature (Lemson & Kauffmann 1999; Avila-Reese et al. 2005; Faltenbacher et al. 2005; Altay et al. 2006; Basilakos et al. 2006; Gottlöber & Turchaninov 2006; Patiri et al. 2006; Aragón-Calvo et al. 2007; Hahn et al. 2007; Macciò et al. 2007; Ragone-Figueroa et al. 2010).

The observational determination of the shapes of dark matter haloes is challenging. Preferably dynamical tracers at large radii are to be used, but these tracers are by definition rare. In external galaxies, constraints on these shapes have been put using the intrinsic shape of galactic discs (Fasano et al. 1993), the kinematics and morphology of the HI layer (Olling 1996; Becaert & Combes 1997; Swaters et al. 1997), the morphology, temperature profile of X-ray isophotes (Buote & Canizares 1998; Buote et al. 2002), gravitational lensing (Hoekstra et al. 2004) and the spatial distribution of galaxies within groups (Robotham et al. 2008) (for earlier reviews on the subject see Rix 1996; Sackett 1999). The general consensus of all these studies is that haloes tend to be roughly oblate, with the smallest axis pointing perpendicular to the symmetry plane defined by the stellar component. Most of these constraints, however, pertain to the inner regions (a few optical radii) of galaxy-scale haloes.

In the case of the Milky-Way, the shape constraints often rely on the kinematics of individual stars, and include e.g. the use of the tilt of the velocity ellipsoid for nearby stars (Siebert et al. 2008), the proper motions of hypervelocity stars (Gnedin et al. 2005) or the dynamics of stellar streams (Koposov et al. 2010). Interestingly, the use of the latter have provided contradictory results, notably in the case of the Sagittarius Stream. For example, the positional information was used to argue that the Milky Way halo is nearly spherical (Ibata et al. 2001; Martínez-Delgado et al. 2004; Johnston et al. 2005) whereas the kinematics of stars in the leading stream could only be fit in a prolate halo elongated perpendicular to the disc (Helmi 2004; Law et al. 2005). More recently, Law et al. (2009); Law & Majewski (2010) have explored triaxial potentials with constant axis ratios, and found models that were able to fit simultaneously these constraints, albeit not completely satisfactorily.

From the theoretical perspective, there is a gap in our knowledge about the way in which dark matter haloes acquire their shape, and in particular, on the impact of the dynamics of the surrounding large scale structure in the non-linear regime (Lee et al. 2005; Betancort-Rijo & Trujillo 2009; Rossi et al. 2010; Salvador-Solé et al. 2011). Indeed, most of the theoretical works cited above restrict their analysis to the present day correlations with the environment,

and do not consider when the shapes have been established and how they relate to the past history of an object. In this paper we use state-of-the-art high resolution  $N$ -body simulations that track the formation of five  $\sim 10^{12}M_{\odot}$  Milky Way-like haloes in a fully cosmological context, in order to gain further understanding of this problem.

This paper is organized as follows. In Section 2 we describe the simulations used in this work which are part of the Virgo Consortium’s *Aquarius* project, and test in Section 3 the convergence of halo shapes for different resolutions. The shapes at the present day, evolution and their relation with the formation history of the dark matter haloes are analyzed in Section 4 and 5. Finally, we discuss and summarize our main conclusions in Section 6. For completeness, we compare in Appendix A the results obtained by using several different schemes to determine halo shapes. Also a novel method for measuring the size of the filaments based on dynamical arguments is described in Appendix B.

## 2 NUMERICAL SIMULATIONS

We use the Aquarius Simulations, a suite of high resolution  $N$ -body cosmological simulations of six Milky Way sized dark matter haloes (Springel et al. 2008). These haloes were selected from a larger  $\Lambda$ CDM cosmological box of  $100h^{-1}$  Mpc side with parameters  $\Omega_m = 0.25$ ,  $\Omega_{\Lambda} = 0.75$ ,  $\sigma_8 = 0.9$ ,  $n_s = 1$  and  $H_0 = 100h$  km s $^{-1}$ Mpc $^{-1} = 73$  km s $^{-1}$ Mpc $^{-1}$ . The Aquarius haloes, labeled **Aq-A** to **Aq-F**, have a final mass  $\sim 10^{12}M_{\odot}$  and were chosen to be relatively isolated at redshift  $z = 0$ . The selection procedure was otherwise random, which allows us to study the impact of different assembly histories on the shape of Milky Way sized dark matter haloes.

Each halo has been re-simulated at various resolution levels that accurately replicate the power-spectrum and phases for the resolved structures in all runs. Following the notation introduced in previous papers, we refer to each level of resolution as -5 to -1, for the lowest to highest resolution. The mass per particle varies from  $m_p = 2.94 \times 10^6 h^{-1}M_{\odot}$  in the level 5 to  $m_p = 1.25 \times 10^3 h^{-1}M_{\odot}$  for the highest resolution run, which resolves a given halo with approximately half-million up to 1.5-billion particles within the virial radius for level 5 and 1, respectively<sup>1</sup>. The results discussed in this paper pertain mostly to the 4th level of resolution ( $m_p \sim 2 \times 10^5 h^{-1}M_{\odot}$ ,  $n_{\text{vir}} \sim 10^6$  particles within  $r_{\text{vir}}$ , gravitational softening  $\epsilon = 250h^{-1}$  pc) of haloes **Aq-A** to **Aq-E** and aim to target the possible structure of the Milky Way dark matter halo. The Aquarius halo **Aq-F** is not considered in this work because it experiences a major merger less than  $\sim 5$  Gyr ago; this is unlikely to be consistent with our current view of the assembly of the Milky Way halo, expected to have had no major mergers since  $z \sim 1$  (Toth & Ostriker 1992).

In this context, this paper focuses on dark matter haloes

<sup>1</sup> Throughout this paper we refer to the virial radius,  $r_{\text{vir}}$ , as the spherical radius that contains a mean density equal to 200 times the critical density of the Universe at a given time. Other virial quantities, such as mass and velocities,  $m_{\text{vir}}$  and  $v_{\text{vir}}$  respectively, correspond to those measured within  $r_{\text{vir}}$ .

Halo	$m_p$	$r_{\text{vir}}$	$m_{\text{vir}}$	$n_{\text{vir}}/10^6$	$r_{\text{conv}}$
Aq-A-4	2.87	179.36	1.34	4.68	2.27
Aq-B-4	1.64	137.86	0.61	3.72	2.14
Aq-C-4	2.35	177.89	1.31	5.58	2.07
Aq-D-4	1.95	177.83	1.31	6.69	2.14
Aq-E-4	1.90	155.95	0.88	4.64	2.05

**Table 1.** Numerical details of the Aquarius haloes for resolution level-4. Each column lists: (1) the name of the halo, (2) mass per particle  $m_p$  in  $10^5 M_\odot h^{-1}$ , (3) the virial radius  $r_{\text{vir}}$  in  $\text{kpc } h^{-1}$  and (4) virial mass  $m_{\text{vir}}$  in  $10^{12} M_\odot h^{-1}$  at  $z = 0$ , (5)  $n_{\text{vir}}$  the number of dark matter particles within  $r_{\text{vir}}$ , (6)  $r_{\text{conv}}$  the convergence radius in  $\text{kpc } h^{-1}$ . The gravitational softening length is  $\epsilon = 250 h^{-1} \text{ pc}$  for all haloes at this resolution level.

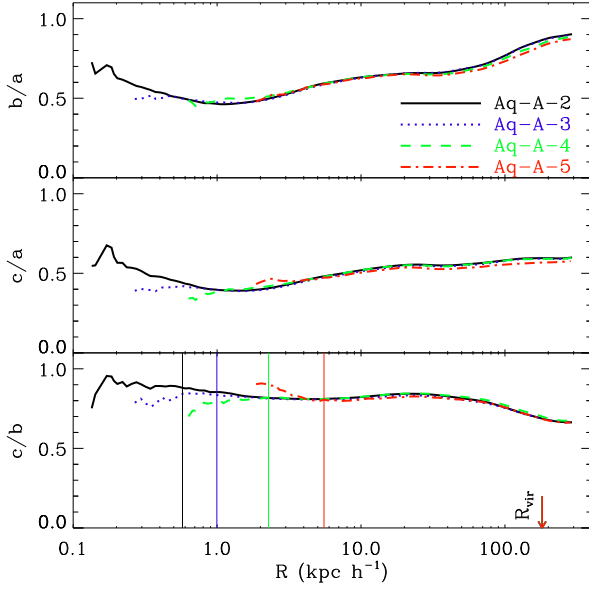


**Figure 1.** Convergence in the axis ratios for the Aq-A halo at four different numerical resolutions. The agreement is remarkable showing that the method used provides reliable axis ratios down to the “convergence radius”  $r_{\text{conv}}$  (denoted by the vertical lines).

with a relatively quiescent merger history (mass ratios lower than 1:5) after  $z \sim 2$  (for a detailed comparison of the Aquarius haloes’ mass accretion history with respect to the general expectations for haloes of similar virial mass see Boylan-Kolchin et al. 2010). We summarize the most relevant numerical details of our haloes at level 4 in Table 1, and we refer the interested reader to Springel et al. (2008) for further information.

### 3 HALO SHAPE DETERMINATION AND CONVERGENCE

Various methods have been introduced in the literature to measure the shapes of dark matter haloes. In Appendix A we describe a wide range of these methods in detail, and show that the measured halo shapes agree reasonably well when applied to the same object. Throughout this article we use the “reduced” inertia tensor method as implemented recently by Allgood et al. (2006). This tensor is defined as

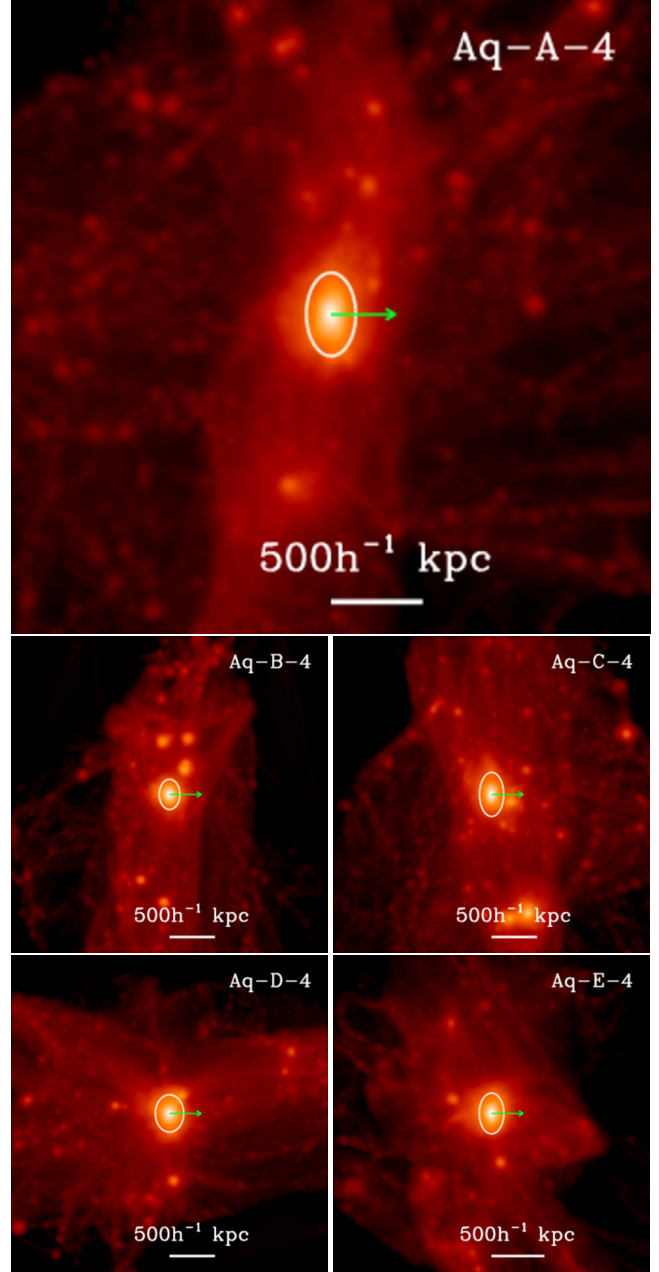


**Figure 2.** Present day dark matter distribution of the Aquarius haloes and their surroundings. Colors are proportional to the logarithm of the squared dark matter density integrated along the line of sight. In each panel the depth of the projected image is  $1.5 h^{-1} \text{ Mpc}$ . The virial ellipsoid is indicated in each panel with a solid white line and the green arrow shows the direction of the minor axis of the halo at the virial contour. The system is orientated such that the minor axis points horizontally and the major axis points vertically.

$$I_{ij} = \sum_{\mathbf{x}_k \in V} \frac{x_k^{(i)} x_k^{(j)}}{d_k^2}, \quad (1)$$

where  $d_k$  is a distance measure to the  $k$ -th particle and  $V$  is the set of particles of interest. Assuming that dark matter haloes can be represented by ellipsoids of axis lengths

$a \geq b \geq c$ , the axis ratios  $q = b/a$  and  $s = c/a$  are the ratios of the square-roots of the eigenvalues of  $\mathbf{I}$ , and the directions of the principal axes are given by the corresponding eigenvectors. Initially the set  $V$  is given by all particles located inside a sphere which is re-shaped iteratively using the eigenvalues of  $\mathbf{I}$ . The distance measure used is  $d_k^2 = x_k^2 + y_k^2/q^2 + z_k^2/s^2$ , where  $q$  and  $s$  are updated in each iteration. Furthermore, in the figures below we have removed all bound substructures contained in a halo using the SUBFIND algorithm (Springel et al. 2001). This alleviates the noise and artificial tilting of the ellipsoids that is introduced by such substructures. More details on our implementation can be found in the Appendix A.

We test the convergence of the shape measurements using the different resolutions of the halo Aq-A, from level 5 to level 2. There is an increase of a factor  $\sim 230$  in the number of particles within the virial radius and a factor  $\sim 10$  reduction in gravitational softening from Aq-A-5 to Aq-A-2. Fig. 1 shows the axis ratios as a function of  $R$  for halo Aq-A, where  $R$  is defined as the geometrical mean of the axis lengths  $R = (abc)^{1/3}$ . This quantity then provides a notion of distance to the centre of the ellipsoid with the advantage of being volume invariant. Hereafter, we use  $R$  when referring to quantities measured using ellipsoidal contours, and  $r$  for spherical contours. With this convention,  $r_{\text{vir}}$  is the spherical radius enclosing an average overdensity of 200 times the critical value, whilst  $R_{\text{vir}}$  refers to the ellipsoid enclosing the same overdensity.

The agreement between the different resolutions in Fig. 1 is remarkable at all radii, although small deviations are present in the inner regions where resolution effects are expected to be important. The vertical lines in the lower panel indicate the “convergence radius”  $r_{\text{conv}}$  (Power et al. 2003; Navarro et al. 2010). This radius is defined by setting  $\kappa(r_{\text{conv}}) = t_{\text{relax}}(r_{\text{conv}})/t_{\text{circ}}(r_{\text{vir}}) = 7$ , where  $t_{\text{relax}}$  is the local relaxation time and  $t_{\text{circ}}(r_{\text{vir}})$  corresponds to the circular orbit timescale at  $r_{\text{vir}}$ . This choice ensures that circular velocity profiles for  $r > r_{\text{conv}}$  deviate less than 2.5% from the highest resolution value. Fig. 1 shows that  $r_{\text{conv}}$  provides also a very good estimate for the smallest radius at which the halo shape has converged. Although not explicitly shown, we have tested that the orientation of the ellipsoids is a well defined attribute independent of resolution for  $r_{\text{conv}} < R < R_{\text{vir}}$ .

Our analysis suggests that convergence in halo shapes is achieved in the level 4 from approximately  $2h^{-1}$  kpc onwards (Table 1). We will therefore focus in what follows on the study of the different Aquarius haloes Aq-A to Aq-E at the level of resolution 4, since this yields a robust characterization of the dark matter halo shapes and orientation, while keeping the numerical cost constrained.

## 4 THE SHAPE OF DARK MATTER HALOES

### 4.1 Present day

Fig. 2 shows a snapshot view of the Aquarius haloes and their surrounding environment. The color scale used is proportional to the logarithm of the squared dark matter density integrated along the line of sight, with a projection depth per panel of  $1.5h^{-1}\text{Mpc}$ . All images have been rotated

according to the orientation of the virial contours (indicated by the solid white curve) in such a way that the major and minor axis define the vertical and horizontal direction, respectively.

A careful look at the environment of each object reveals that the Aquarius haloes are all embedded within a filamentary-like structure, which is better defined in some cases than in others (e.g. Fig. 2 Aq-A vs Aq-E), a result that holds independently of the projection used. These filaments also seem to contain the most massive substructures in the box and interestingly, the minor axes of the virial contours tend to be perpendicular to the direction defined by these. This is in very good agreement with the statistical findings of Bailin & Steinmetz (2005), who analyzed a sample of  $\sim 4000$  haloes in a wide range of masses. One relevant consequence of this type of configuration is that most of the substructure will preferentially be accreted along the *major* axis of the halo, a feature that has been used to explain the preferential alignment of satellite galaxies with respect to their hosts in observational studies of external galaxies (e.g. Brainerd 2005, and references therein), in groups (e.g. Binggeli 1982; Kitzbichler & Saurer 2003; Yang et al. 2006; Faltenbacher et al. 2007; Godłowski & Flin 2010; Paz et al. 2011) and also numerical simulations (e.g. Knebe et al. 2004; Libeskind et al. 2005, 2007; Kang et al. 2007; Sales et al. 2007; Bailin et al. 2008; Faltenbacher et al. 2008; Libeskind et al. 2011).

The halo shapes and orientations as a function of radius are shown in Fig. 3. On the right panel, besides the axis ratios, we also plot the triaxiality parameter  $T$  defined as

$$T = \frac{a^2 - b^2}{a^2 - c^2}, \quad (2)$$

which is unity for a perfect prolate distribution and zero in the oblate case (Franx et al. 1991; Warren et al. 1992). This figure shows that in the inner regions all dark matter haloes are more “prolate” with  $b/a \sim c/a \sim 0.4\text{--}0.6$  (Hayashi et al. 2007). On the other hand, at large radii  $b/a$  increases to  $0.8\text{--}0.9$ , and the mass distribution becomes more oblate/triaxial. At intermediate radii haloes are typically triaxial, but notice that the radius at which the prolate-to-oblate transition occurs (defined as the radius where  $T = 0.5$ ) is different for each object, ranging from  $\sim 20h^{-1}$  kpc for Aq-E to  $\sim 100h^{-1}$  kpc in the case of Aq-A.

Regardless of the change in shape of the concentric ellipsoids, these tend to remain well aligned throughout the halo. The right panel of Fig. 3 shows the cosines of the relative angle between the major, intermediate and minor axis of the ellipsoids at different radii and at the virial contour. The alignment is remarkable, with the exception of halo Aq-D, where the intermediate and minor axis in the inner regions are rotated  $\sim 60^\circ$  with respect to their orientation at the virial radius, an issue that we explore in the next section.

### 4.2 Evolution

Fig. 4 shows a series of snapshots of halo Aq-D at different stages of its evolution. The orientation of the coordinate system is now kept fixed for all the snapshots. The corresponding time is quoted in the upper left corner of each panel, the virial ellipsoids are depicted by white ellipses while the pro-

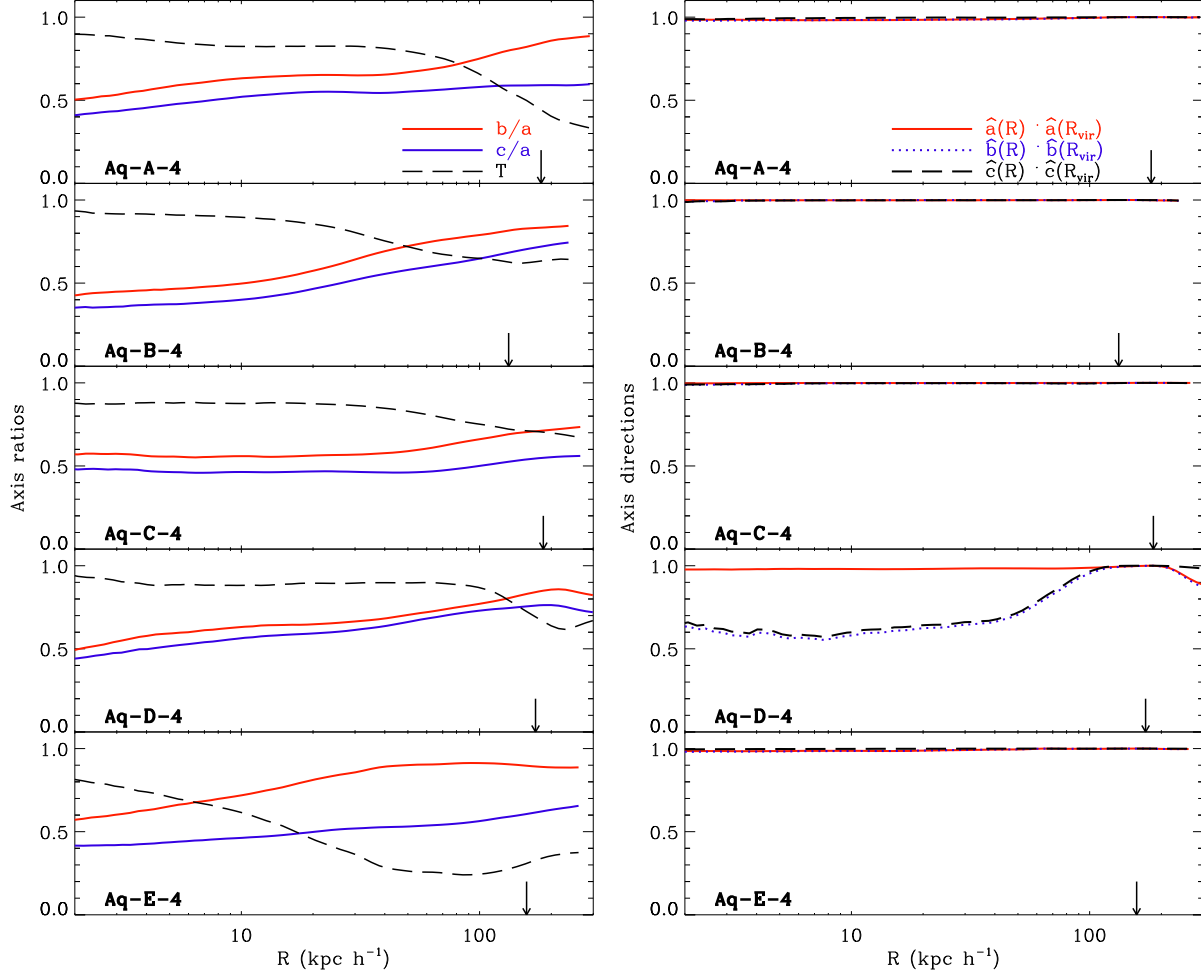


**Figure 3.** Axis ratios (left) and directions (right) as a function of  $R$  for each of the Aq-haloes. In the left panels the thick solid lines represent the axis ratios  $b/a$  (red) and  $c/a$  (blue), while the dashed curves are the triaxiality parameter  $T$ . In general haloes are more prolate in the inner parts and more oblate (and triaxial) in the outskirts. All concentric shells are also strongly aligned with the exception of halo Aq-D which exhibits a clear twisting close to the virial radius.

jection of the minor axes onto the plane are indicated by the green arrows. There are several points worth highlighting:

- The shape and orientation of the halo seem to change throughout time (with the caveat that we are just seeing its evolution in *projection*).
- Also evident from this figure is the filamentary structure that characterizes the surroundings of Aq-D. Notice that the filament where this halo is located at the present day was already in place at  $t \lesssim 1$  Gyr, and fully dominates the environment from  $t \sim 3$  Gyr onwards, with remarkable coherence in time and direction.
- The relative orientation of halo Aq-D with respect to its environment is interesting since its minor axis is *parallel* to the direction of the filament at late times. This seems to be at odds with expectations from statistical studies of dark matter halo alignments (Bailin & Steinmetz 2005; Faltenbacher et al. 2005; Aragón-Calvo et al. 2007; Zhang et al. 2009) as well as in contradiction with the other haloes illustrated in Fig. 2 and the analysis presented in Section 4.1. A closer inspection of the history of this halo shows that the infall of material at  $t \gtrsim 7.5$  Gyr occurs mostly along a sec-

ondary filament (only barely visible in this projection) whose direction is almost perpendicular to that of the most prominent and massive filament that dominates the surrounding large scale structure and is clearly seen in Fig. 4. This change of infall direction explains the apparent change in orientation of halo Aq-D at late times.

- The relative size of a filament with respect to that of the halo increases with time: the filament’s cross section is comparable to the virial radius at  $t \lesssim 5$  Gyr, whereas the dark matter halo becomes smaller than and is fully embedded in the filament at later times. This has interesting consequences on the halo shape as we discuss further in Section 5. We have explicitly checked that this conclusion is not dominated by projection effects nor rendering of our images. We refer the reader to Appendix B, where we introduce a physically motivated definition of a filament (based on the number of caustic-crossings a particle has experienced) and compare its size with that of the halo at each timestep.

In Fig. 5 we quantify the time evolution of the axis ratios measured at the instantaneous virial ellipsoids for haloes Aq-A to Aq-E. For reference, we have indicated with grey la-



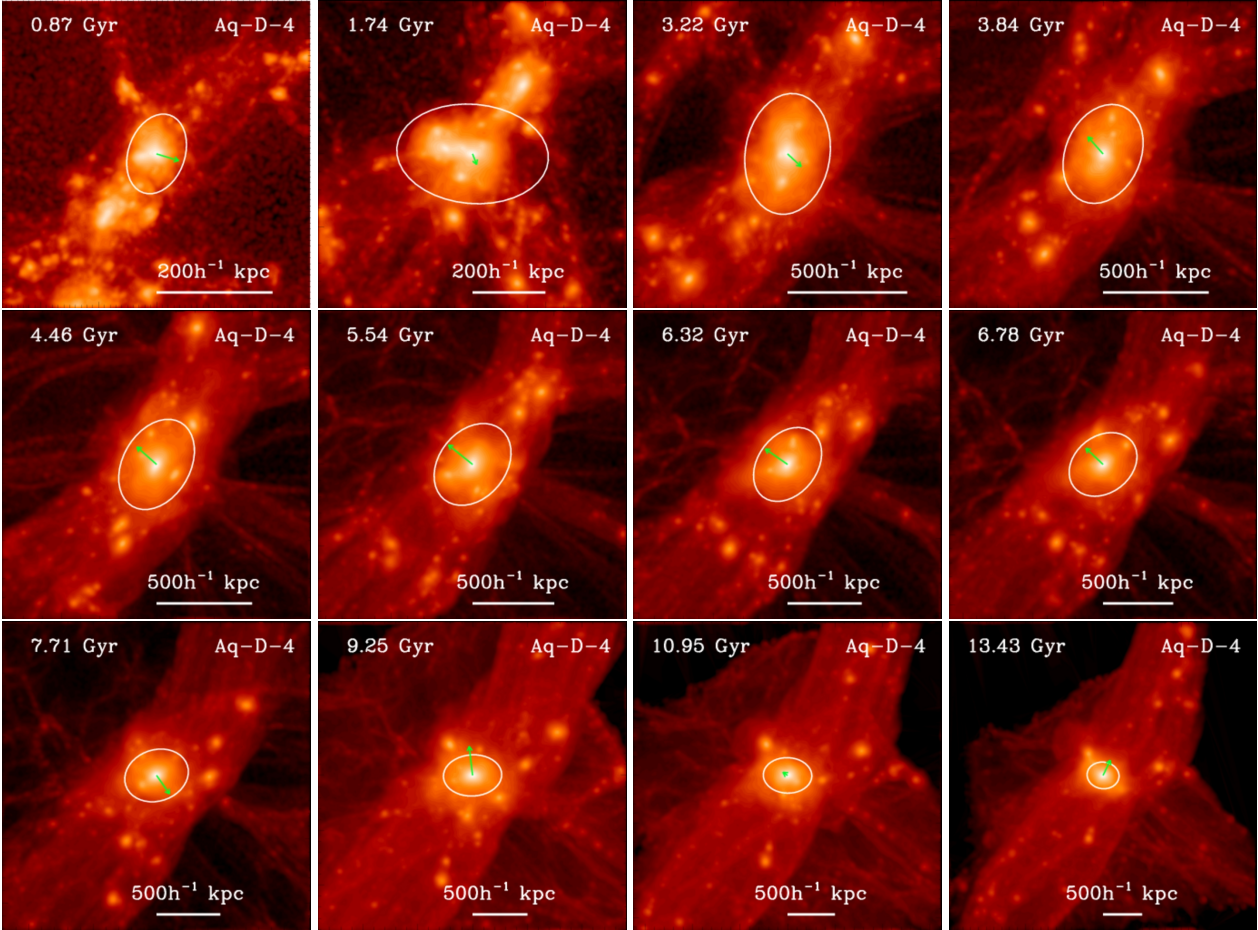


**Figure 4.** Time sequence of the formation of halo Aq-D from  $t \sim 1$  Gyr to the present day. Each box shows the dark matter density distribution around this halo together with the shape and orientation of the virial contour at the given time. As before, the green arrows indicate the projection of the minor axis onto the plane, with the length of the arrow being proportional to the minor axis length. The shape of this halo evolves continuously with time, showing stretching and tilting in response to the infall of matter. The halo is oriented along the filament up to  $t \sim 7$  Gyr and then rotates and becomes perpendicular to it at the present day. This figure clearly illustrates the complexity involved in the build up of the present day dark matter halo’s structure.

bels the corresponding physical sizes at a given time. We will only follow the evolution from  $t = 2$  Gyr onwards (which corresponds roughly to the time at which the haloes have  $\sim 20\%$  of their final mass), which guarantees that the centre of mass as well as the shapes at the virial radius are well defined at all times for the full sample of haloes.

Fig. 5 shows that the shape of the virial ellipsoids is not constant with time. In general, haloes seem to evolve from a quite prolate configuration at early times towards more triaxial shapes at the present day. In most of our haloes (with the exception of Aq-D), this evolution in shape is driven by a larger increase of the intermediate-to-major axis ratio  $b/a$  than in  $c/a$ . Except for this weak general trend, the evolution of the axis ratios is quite disparate from halo to halo.

A qualitative comparison between the left panel of Fig. 3 and 5 suggests a certain degree of resemblance between the overall evolution of the virial ellipsoid’s shape with time (as measured, for example, by the triaxiality parameter) and the shapes measured as a function of radius (Fig. 3) for each of our haloes, despite their intrinsic differences. This suggests that the dark matter haloes retain certain *memory* of their configuration in the past, and that this is imprinted

on their present day structure. We note however that this refers to the overall *trend* with radius/time and does not imply that it is possible to recover the *exact* numerical value of the axis ratios at a given time from their present day value at a given radius.

This analogy between radius/time is better seen in Fig. 6, where we plot the present day axis ratios  $b/a$  vs  $c/a$  at different radii (grey curve) as well as those measured at the virial ellipsoids for different times (color points). Because we sample from  $t = 2$  Gyr onwards, a dotted or a solid line is used to indicate respectively, the shapes at radii smaller or larger than the virial ellipsoid  $R_{\text{vir}}$  at this time. This figure shows that haloes evolve away from the 1:1 line and therefore tend towards less prolate shapes with time (and also radius), with the clear exception of halo Aq-D. Moreover, the reasonable agreement between the solid curve and the diamonds in this figure suggests that the present day shape of the dark matter haloes at different radii provides information about the evolution of the virial ellipticities during their assembly history.

The analysis presented in this section, if generalized to Milky Way-type haloes, is directly relevant to the modeling

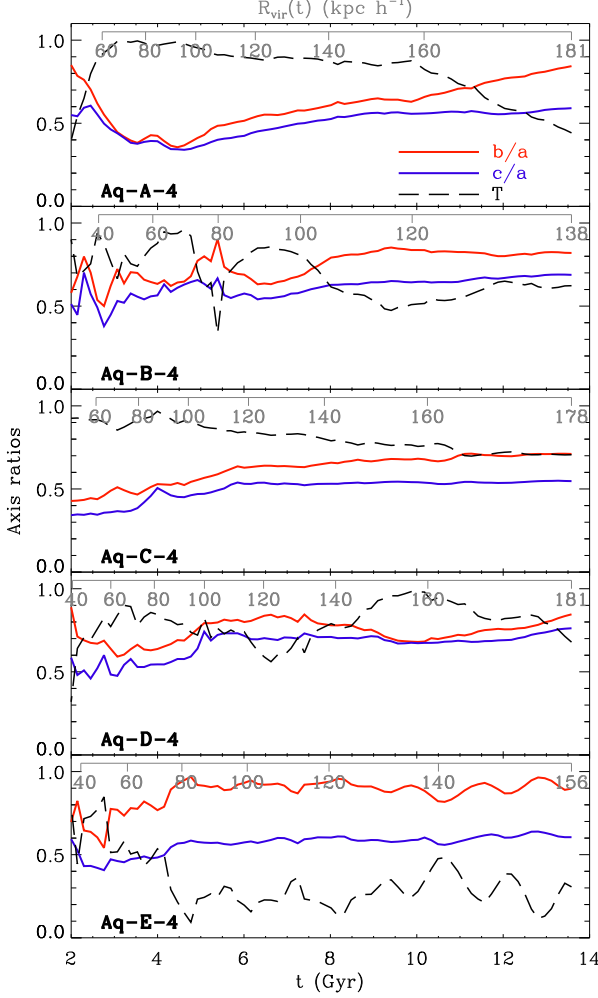


**Figure 5.** Temporal evolution of the axis ratios and triaxiality parameter for the virial contour. The color-coding is the same as in Fig. 3. A comparison to that figure shows that a correlation exists between the shape as a function of time, and the present-day shape as a function of radius. To aid this comparison we have added a second axis (gray), indicating the size of the virial contour  $R_{\text{vir}}$ . This is derived for each halo by fitting:  $R_{\text{vir}}(t) = A(1 - e^{-(t-\tau)/(2t_h)})$  to the measured evolution of the virial (ellipsoidal) radius. Here  $t_h$  is the time at which the virial mass reaches half its present value, and  $A$  and  $\tau$  are free parameters.

and interpretation of observational constraints on the shape of the Galactic potential. As discussed in the Introduction, the Sagittarius stream has led to contradictory results when modeled in axisymmetric dark matter haloes with constant axis ratios (in the potential) (Ibata et al. 2001; Helmi 2004; Law et al. 2005; Johnston et al. 2005; Fellhauer et al. 2006). We have shown here that significant variations in the axis ratios as a function of radius exist for all our five Aquarius haloes and those variations are linked to the evolutionary history of each object. Although this might add an extra degree of freedom to models that attempt to constrain the Galactic potential, our results from Fig. 6 indicate that by doing so it may be possible to retrieve the local conditions around the Milky Way’s halo throughout its assembly (Banerjee & Jog 2011).

## 5 ENVIRONMENT, MASS ACCRETION AND HALO SHAPES

Dark matter haloes continue to grow with time, through a regular, although not always steady, injection of matter. Halos will respond to this new material and re-structure themselves onto a new equilibrium configuration as part of the virialization process. The environment of an object determines to some extent the way in which the material is incorporated into the halo. For instance, thin filaments imply accretion through well-defined preferential directions whereas a more isotropic mode is expected when the halo is embedded in a larger structure. Several correlations of halo shapes with environment have been found so far in simulations (e.g. Avila-Reese et al. 2005; Faltenbacher et al. 2005; Patiri et al. 2006; Basilakos et al. 2006; Macciò et al. 2007; Hahn et al. 2007) and observations (e.g. Pimbblet 2005; Godłowski & Flin 2010; Niederste-Ostholt et al. 2010; Paz et al. 2011), albeit with significant scatter. In this section we explore in detail the role played by the environment and mass assembly histories in shaping the Aquarius haloes.

The angular distribution on the sky of the infalling matter can provide useful information about the preferred directions and modes of the ongoing accretion (Tormen 1997; Colberg et al. 1999; Aubert et al. 2004; Aubert & Pichon 2007; Libeskind et al. 2011). For instance, whereas isotropic accretion would lead to a uniform signal on the sky, the presence of a thin filament will give rise to a bi-modal distribution of points in two opposite ( $180^\circ$  apart) directions. This can be quantified further by means of a multipole expansion of the infalling particles on the sky at a given time. We measure the power spectrum for the mode  $l$  as,

$$C_l = \frac{1}{4\pi} \frac{1}{2l+1} \sum_{m=-l}^l |\tilde{a}_l^m|^2, \quad (3)$$

where the expansion coefficients are,

$$\tilde{a}_l^m = \frac{m}{4\pi r_{\text{vir}}^2} \sum_{k=1}^N (Y_l^m(\Omega_k))^*, \quad (4)$$

with  $\Omega_k$  being the angular position of the  $k$ -th particle crossing the virial radius  $r_{\text{vir}}$  with negative radial velocity at any given time. The asterisk on the right hand side of Eq. (4) indicates the complex conjugate of the term within parenthesis.

In the scheme introduced above, the  $l = 0$  term (monopole) is a constant equal to unity and used for the overall normalization of the expansion. Notice that although this choice is arbitrary, the *relative* relevance of the monopole with respect to all the other modes,  $C_0/\sum_l C_l$ , is an indication of how isotropic the distribution is; i.e. a perfectly isotropic infall would correspond to all the power in the  $l = 0$  term. On the other hand, a significant contribution of the  $l = 2$  (or quadrupolar moment) term arises when the accretion occurs through a well-defined direction in space, i.e. a filament. Similarly, accretion corresponding to more than one preferential direction will shift the power away from  $l = 2$  and towards higher moments. Notice that a point mass on the sky will excite, by definition, a wide range of modes with similar power; just like the Fourier transform

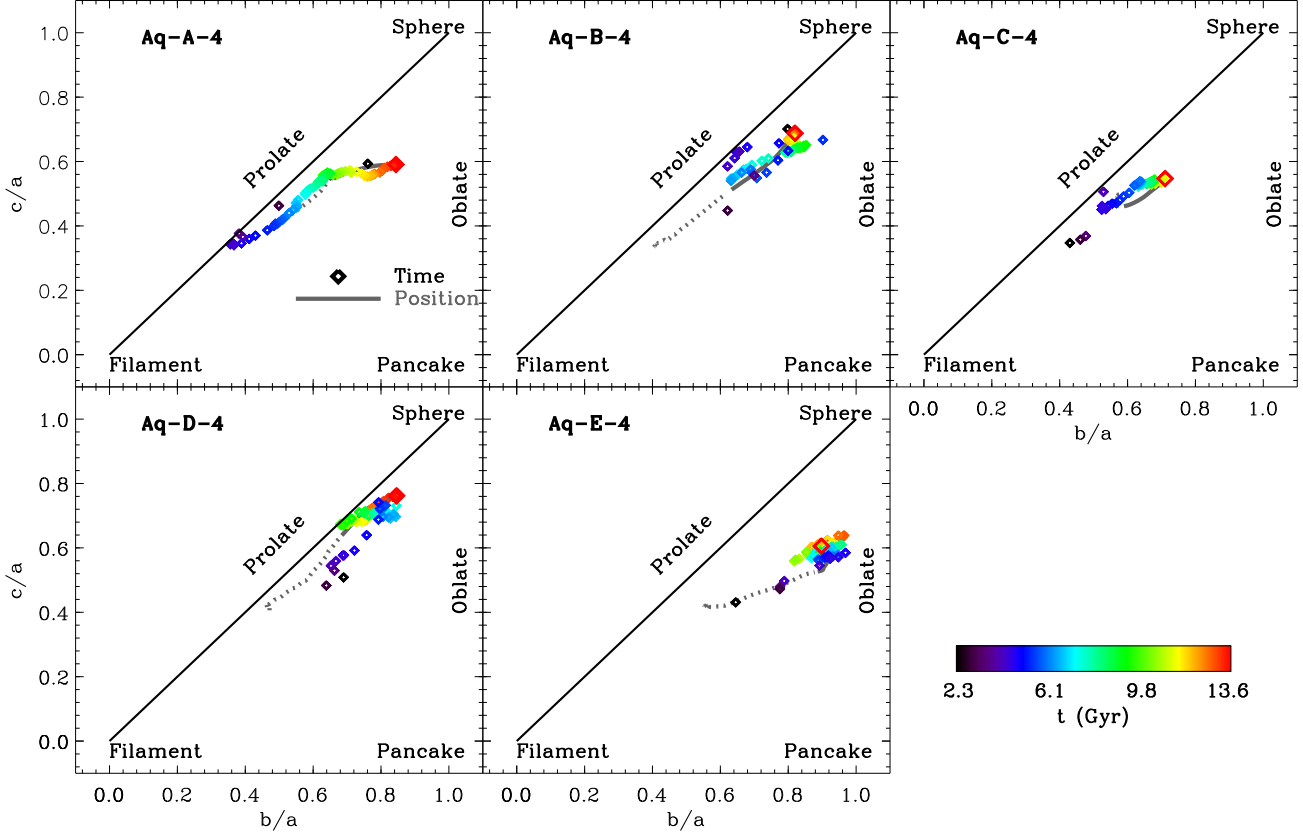


**Figure 6.** Axis ratios as a function of position (gray line) and time (diamonds). The colors indicate the time when the axis ratios at the virial contour have been measured. Notice that since we consider temporal evolution only after  $t = 2$  Gyr, we have differentiated the shape as a function of position (gray curve) using solid (dotted) lines for distances larger (smaller) than the virial radius of each halo at  $t = 2$  Gyr (see text for details).

of a Dirac-delta function has constant power for all modes in the frequency space. We therefore expect single satellite infall events to excite higher moments compared to the smooth accretion. In the limit of a satellite that occupies a large area of the sky, the configuration will then resemble a dipole and the power spectrum will exhibit high power in the  $l = 1$  mode.

In practice, most of the information is encoded in the terms  $l \leq 2$  (e.g. Quinn & Binney 1992; Eisenstein & Loeb 1995; Aubert et al. 2004). We have checked in our experiments that higher moments than quadrupolar contribute always less than  $\sim 15\%$  of all power at any given time once substructures have been removed. We therefore focus our analysis mostly on the  $l = 0$  and  $l = 2$  moments since they provide most of the information that allow to characterize the mass accretion onto dark matter haloes.

Fig. 7 shows this multipole decomposition introduced in Eq. (3) of the mass infalling onto Aq-A-4 as a function of time. At each output time, we select particles with negative radial velocity (infalling),  $v_r < 0$ , that are in the spherical shell  $1.0 \leq r/r_{\text{vir}} \leq 1.2$  and compute the corresponding  $C_l$  of the distribution<sup>2</sup>. The upper and the middle panels of this figure show the  $C_l$  power spectra obtained respectively,

by including and by removing particles associated with substructures as identified by SUBFIND. Both distributions are quite similar, although as expected from the discussion in the previous paragraph, satellite accretion excites in general higher modes that last a very short timescale, and are visible as clear “spikes” in the upper panel of the figure.

The virialized regions of galaxy-sized objects can extend well beyond their formal  $r_{\text{vir}}$  (e.g. Cuesta et al. 2008), introducing a signal in the power spectrum that is driven by the halo’s intrinsic shape rather than by the surrounding infall pattern. In order to avoid confusion with the material already in place and in equilibrium in the outskirts of the halo, we selected also the subsample of particles within  $1.0 \leq r/r_{\text{vir}} \leq 1.2$  that are infalling for the *first time* onto the halo (in practice we do this by requiring that a particle in a given output has never been within the virial radius of the main object at any previous time step). The corresponding power spectrum (after removing the subhaloes’ contribution) is shown in the bottom panel of Fig. 7. This distribution agrees well with those shown in the other panels of this figure, although the features appear noisier due to the smaller number of particles being considered.

The left panel of Fig. 8 shows the power spectrum of

<sup>2</sup> We have tested that the qualitative behavior shown in this figure and the relative relevance of each mode with respect to the

whole spectrum does not depend on the particular shell that is analyzed for  $1 < r/r_{\text{vir}} < 2$  for all of our haloes.



all infalling material for all five Aquarius haloes after the contribution from subhaloes has been removed. The residual “spikes” visible in this figure correspond to the matter that is associated to infalling substructures but that is rather loose and, consequently, has not been assigned to a particular subhalo by the halo finder.

The right panel of Fig. 8 shows the relative contribution of the  $l = 2$  (solid black curve) and  $l = 0$  (blue dot-dashed) moments to the total power spectrum as a function of time<sup>3</sup>. These have been computed using only the subset of particles on their first infall (although these curves do not change significantly when all infalling particles are considered instead). Large  $C_2$  values are associated with the presence of net filamentary accretion. Fig. 8 shows that this condition is typically found at early times in our haloes, with the exception of Aq-B, which shows no clear sign of smooth accretion through a filament at any time. The halo Aq-D shows also a peculiarly high power in the  $l = 2$  mode at late times, whereas for most of the objects the relevance of  $C_2$  remains approximately flat (and negligible) in the last few Gyr (a feature which is also evident in the left panel of Fig. 8).

The monopole term largely dominates the accretion at later times (blue dot-dashed curve in Fig. 8) in all haloes. Exceptions are haloes Aq-A and Aq-D, which show a decline in  $C_0/\Sigma C_l$  beyond  $t \sim 12$  Gyr and  $t \sim 10$  Gyr respectively. In the case of Aq-A this is related to an increase in power of  $l \geq 2$  modes, while for Aq-D this is driven only by the  $l = 2$  moment, as mentioned in the previous paragraph. As we show in Appendix B, this more isotropic infall is a direct consequence of the increase in the relative size of the filaments feeding the dark matter haloes: infalling particles cover wider angles on the sky which leads to larger  $C_0$  contributions with negligible  $l = 2$  component. Notice that halo Aq-E is, in some sense, the most extreme object, with a monopolar term that dominates the power spectrum of infall material during almost all its entire history ( $C_0/\Sigma_l C_l > 0.9$  for  $t \sim 3$  Gyr onwards).

A careful comparison of Fig. 8 and Fig. 5 reveals a good correlation between the infall of material through filaments (large  $C_2$ ) and the shape of the haloes at a given time: high  $l = 2$  moments are associated with virial contours that turn prolate (e.g. Aq-A for  $t < 6$  Gyr, Aq-C for  $t < 4$  Gyr, Aq-D for  $t > 8$  Gyr). In particular, this multipole decomposition shows a filamentary accretion mode for halo Aq-D that is present at  $t \geq 10$  Gyr, helping to explain why its axis ratio  $b/c$  remains close to unity at quite late times. When the accretion is more isotropic (i.e.  $C_0/\Sigma_l C_l \simeq 0.9$ ), the haloes become most nearly oblate. This explains why halo Aq-E is the more oblate in our sample, with  $b/a \sim 0.9$  from  $t \sim 3.5$  Gyr onwards, and also why it has this shape at smaller radii, compared for example to halo Aq-C.

We found that *the injection of material that occurs along filaments leads to a more prolate halo shape, an effect that is naturally enhanced at early times due to the relatively smaller size of the filaments with respect to the dark mat-*

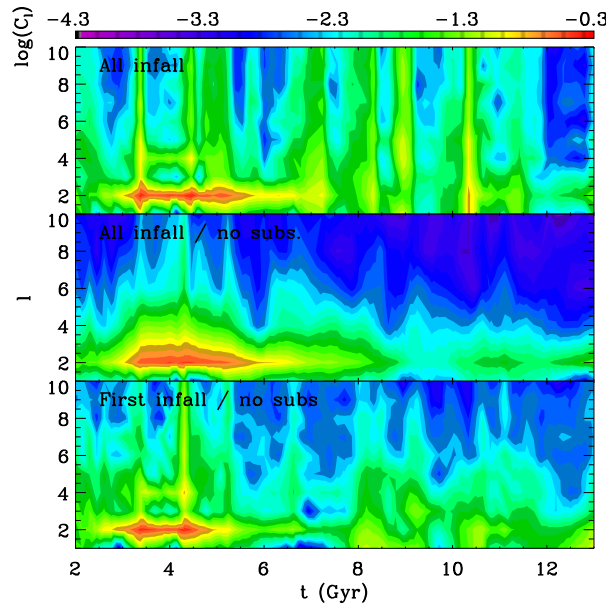


**Figure 7.** Multipole expansion of the infalling material ( $v_r < 0$ ) in the region  $1.0 \leq r/r_{\text{vir}} \leq 1.2$  as a function of time for halo Aq-A–D. The upper and middle panels show the results with and without the contribution from subhaloes, respectively. In the bottom panel only those particles that are on their *first infall* have been considered.

ter halo (Avila-Reese et al. 2005; Gottlöber & Turchaninov 2006). On the other hand, the more isotropic mass accretion that characterizes later phases of halo assembly for  $10^{12}M_\odot$  Milky Way-like objects, yields more oblate/triaxial geometries. When combined with the *memory* effect alluded to in Section 4.2, we find that prolate shapes are naturally expected to be set in the earliest collapsed regions (small radii) of  $\sim 10^{12}M_\odot$  haloes, in good agreement with previous work (Bailin & Steinmetz 2005; Hayashi et al. 2007). The filamentary structure typically found at early times thus seems to be responsible for the general trend of our Milky Way-like haloes to be more prolate in their inner regions.

## 6 CONCLUSIONS

In this paper we analyzed the shape of five Milky Way-like dark matter haloes selected from the Aquarius  $N$ -body simulations. We compared the performance of several methods proposed in the literature to measure the shapes of haloes and found good agreement between all techniques, especially in the inner regions where substructures play only a minor role. Using an implementation of the normalized inertia tensor algorithm described in Allgood et al. (2006), we have found excellent convergence between the several resolution levels of Aquarius, where the shapes can be robustly measured down to the convergence radius.

We find that mass assembly and environment are both responsible for setting the shapes of dark matter haloes. The early evolutionary phases of  $10^{12}M_\odot$  Milky Way-like haloes are characterized by the accretion of matter through narrow filaments. In these circumstances the haloes –as measured by their virial contours– are prolate and their minor axes tend to point perpendicular to the infall (filament) direction.

<sup>3</sup> Note that we are not explicitly showing the  $l = 0$  term in Fig. 8 because it is, by definition, set to unity in our formalism. However, the “relative” importance of the monopole with respect to the contribution of all other moments is a well defined quantity, that we analyze in more detail on the right panel of the same figure.

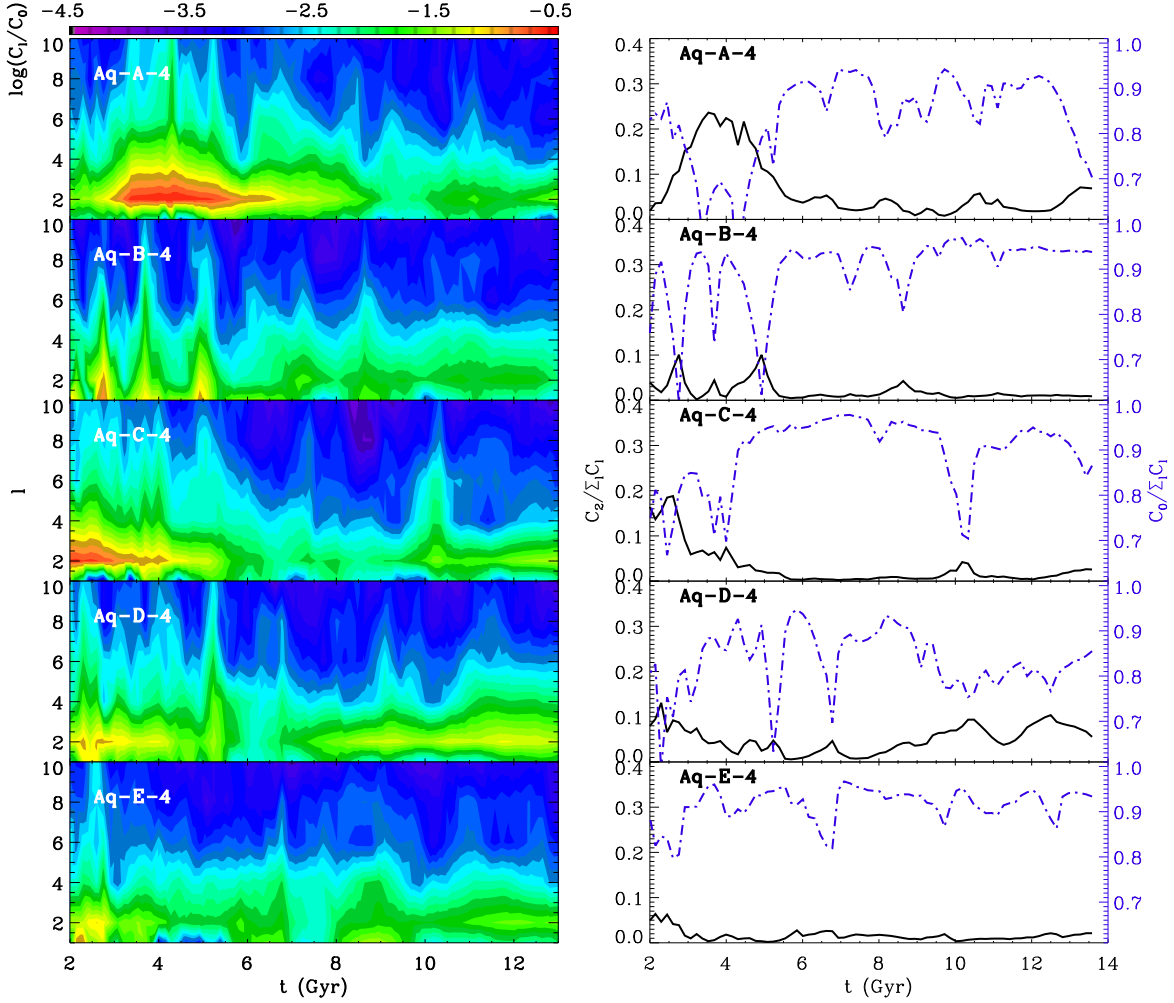


**Figure 8.** *Left:* Multipole expansion of the infalling material in the region  $1.0 \leq r/r_{\text{vir}} \leq 1.2$  as a function of time once the contribution from subhaloes has been removed for the five Aquarius haloes. *Right:* Relative contribution of the  $l = 0$  (blue dot-dashed) and  $l = 2$  (black solid) modes to the total power spectrum as a function of time for particles on their *first infall* onto each halo. While  $C_2/\Sigma_l C_l$  provides information about the material infalling along a filament, large contributions from the monopolar term,  $C_0/\Sigma_l C_l$ , imply that the accretion is isotropic. Notice the good correlation between the time intervals with a clear signature of mass accretion through filaments (high power in  $l = 2$  mode) and the more prolate shape in Fig. 5.

Nonetheless, temporary tilting of the virial ellipsoids may occur when mass is accreted from a different direction. The latter is the case for just one of our haloes located in a well defined filament at redshift  $z = 0$ .

On the other hand, at later times the cross-section of the filaments becomes larger than the typical size of Milky Way-like haloes and as a result, accretion turns more isotropic and the objects evolve into a more oblate/triaxial configuration. This transition does not occur at the same time for all haloes in the explored mass range but is strongly determined by their individual history of mass assembly and their surrounding environment.

The geometrical properties of haloes at different epochs are not lost: haloes retain memory of their structure at earlier times. This memory is imprinted in their present-day shape trends with radius, which change from typically prolate in the inner (earlier collapsed) regions to a triaxial in the outskirts (corresponding to the shells that have collapsed last and are now at the virial radius). These results are in

excellent agreement with previous findings (Bailin & Steinmetz 2005; Hayashi et al. 2007).

A corollary of our results is that the strong link between halo properties and assembly history, which can show large variations from halo to halo, will make any *instantaneous* correlation between haloes shape or orientation and mass or environment rather weak, explaining in part the relatively large scatter in such trends found in earlier studies (e.g. Bailin & Steinmetz 2005; Bett et al. 2007).

It is important to stress that we have neglected the effects induced by the presence of baryons on the dark matter halo shapes (Kazantzidis et al. 2004; Bailin et al. 2005; Gustafsson et al. 2006; Debattista et al. 2008; Pedrosa et al. 2009; Lau et al. 2011; Valluri et al. 2010). Therefore our results may only be directly applicable to dark matter dominated objects such as low surface brightness galaxies. However, the work of Tissera et al. (2010); Abadi et al. (2010); Bett et al. (2010) shows that even though the halo axis ratios

increase when a disc is formed (i.e. they become rounder), the trends with radius appear to be preserved.

With the caveat of the neglected baryonic effects and the relatively low number of objects studied, our findings may be directly relevant to the modeling of stellar streams used to determine the gravitational potential of the Milky Way. For example, the inconsistencies found between the constraints imposed by the positions and by the kinematics of stars in the Sagittarius stream could be indicative of a change in the shape of the Milky Way halo with radius (although see Law et al. 2009; Law & Majewski 2010). Such a change could in principle be measured by using stellar streams which are on different orbits in the Galactic halo. Furthermore, it may even be possible to employ these to determine the growth history and early environment of the Milky Way. A validation of these ideas, however, is bound to a proper evaluation of the effect of the baryonic matter on our findings, as well as to the study of larger statistical samples, both issues that we plan to address in the near future.

## ACKNOWLEDGMENTS

LVS and AH gratefully acknowledge financial support from NWO and from the European Research Council under ERC-Starting Grant GALACTICA-240271. CSF acknowledges a Royal Society Wolfson Research Merit Award. This work was supported in part by an STFC rolling grant to the Institute for Computational Cosmology at Durham. We thank the anonymous referee for useful suggestions and comments.

This paper has been typeset from a  $\text{\LaTeX}$  file prepared by the author.

## REFERENCES

- Abadi M. G., Navarro J. F., Fardal M., Babul A., Steinmetz M., 2010, *MNRAS*, 407, 435
- Allgood B., Flores R. A., Primack J. R., Kravtsov A. V., Wechsler R. H., Faltenbacher A., Bullock J. S., 2006, *MNRAS*, 367, 1781
- Altay G., Colberg J. M., Croft R. A. C., 2006, *MNRAS*, 370, 1422
- Aragón-Calvo M. A., Jones B. J. T., van de Weygaert R., van der Hulst J. M., 2007, *A&A*, 474, 315
- Aragón-Calvo M. A., van de Weygaert R., Jones B. J. T., van der Hulst J. M., 2007, *ApJ*, 655, L5
- Aubert D., Pichon C., 2007, *MNRAS*, 374, 877
- Aubert D., Pichon C., Colombi S., 2004, *MNRAS*, 352, 376
- Avila-Reese V., Colín P., Gottlöber S., Firmani C., Mautsches C., 2005, *ApJ*, 634, 51
- Avila-Reese V., Colín P., Valenzuela O., D’Onghia E., Firmani C., 2001, *ApJ*, 559, 516
- Bailin J., Kawata D., Gibson B. K., Steinmetz M., Navarro J. F., Brook C. B., Gill S. P. D., Ibata R. A., Knebe A., Lewis G. F., Okamoto T., 2005, *ApJ*, 627, L17
- Bailin J., Power C., Norberg P., Zaritsky D., Gibson B. K., 2008, *MNRAS*, 390, 1133
- Bailin J., Steinmetz M., 2005, *ApJ*, 627, 647
- Banerjee A., Jog C. J., 2011, *ApJ*, 732, L8+
- Basilakos S., Plionis M., Yepes G., Gottlöber S., Turchaninov V., 2006, *MNRAS*, 365, 539
- Becquaert J., Combes F., 1997, *A&A*, 325, 41
- Bertschinger E., 1985, *ApJS*, 58, 39
- Betancort-Rijo J. E., Trujillo I., 2009, preprint (ArXiv:0912.1051)
- Bett P., Eke V., Frenk C. S., Jenkins A., Helly J., Navarro J., 2007, *MNRAS*, 376, 215
- Bett P., Eke V., Frenk C. S., Jenkins A., Okamoto T., 2010, *MNRAS*, 404, 1137
- Binggeli B., 1982, *A&A*, 107, 338
- Binney J., Tremaine S., 2008, *Galactic Dynamics: Second Edition*. Princeton University Press
- Boylan-Kolchin M., Springel V., White S. D. M., Jenkins A., 2010, *MNRAS*, 406, 896
- Brainerd T. G., 2005, *ApJ*, 628, L101
- Bullock J. S., 2002, in P. Natarajan ed., *The Shapes of Galaxies and their Dark Halos Shapes of Dark Matter Halos*. pp 109–113
- Buote D. A., Canizares C. R., 1998, *MNRAS*, 298, 811
- Buote D. A., Jeltema T. E., Canizares C. R., Garmire G. P., 2002, *ApJ*, 577, 183
- Colberg J. M., White S. D. M., Jenkins A., Pearce F. R., 1999, *MNRAS*, 308, 593
- Cole S., Lacey C., 1996, *MNRAS*, 281, 716
- Cuesta A. J., Prada F., Klypin A., Moles M., 2008, *MNRAS*, 389, 385
- Davis M., Efstathiou G., Frenk C. S., White S. D. M., 1985, *ApJ*, 292, 371
- Debattista V. P., Moore B., Quinn T., Kazantzidis S., Maas R., Mayer L., Read J., Stadel J., 2008, *ApJ*, 681, 1076
- Diemand J., Moore B., 2011, *Adv. Sci. Lett.*, 4, 297
- Dubinski J., Carlberg R. G., 1991, *ApJ*, 378, 496
- Eisenstein D. J., Loeb A., 1995, *ApJ*, 439, 520
- Faltenbacher A., Allgood B., Gottlöber S., Yepes G., Hoffman Y., 2005, *MNRAS*, 362, 1099
- Faltenbacher A., Jing Y. P., Li C., Mao S., Mo H. J., Pasquali A., van den Bosch F. C., 2008, *ApJ*, 675, 146
- Faltenbacher A., Li C., Mao S., van den Bosch F. C., Yang X., Jing Y. P., Pasquali A., Mo H. J., 2007, *ApJ*, 662, L71
- Fasano G., Amico P., Bertola F., Vio R., Zeilinger W. W., 1993, *MNRAS*, 262, 109
- Fellhauer M., Belokurov V., Evans N. W., Wilkinson M. I., Zucker D. B., Gilmore G., Irwin M. J., Bramich D. M., Vidrih S., Wyse R. F. G., Beers T. C., Brinkmann J., 2006, *ApJ*, 651, 167
- Fillmore J. A., Goldreich P., 1984, *ApJ*, 281, 1
- Franx M., Illingworth G., de Zeeuw T., 1991, *ApJ*, 383, 112
- Frenk C. S., White S. D. M., Davis M., Efstathiou G., 1988, *ApJ*, 327, 507
- Gerhard O. E., 1983, *MNRAS*, 202, 1159
- Gnedin O. Y., Gould A., Miralda-Escudé J., Zentner A. R., 2005, *ApJ*, 634, 344
- Godłowski W., Flin P., 2010, *ApJ*, 708, 920
- Gottlöber S., Turchaninov V., 2006, in G. A. Mamon, F. Combes, C. Deffayet, & B. Fort ed., *EAS Publications Series Vol. 20 of EAS Publications Series, Halo Shape and its Relation to Environment*. pp 25–28
- Gunn J. E., Gott III J. R., 1972, *ApJ*, 176, 1
- Gustafsson M., Fairbairn M., Sommer-Larsen J., 2006, *Phys. Rev. D*, 74, 123522

- Hahn O., Carollo C. M., Porciani C., Dekel A., 2007, *MNRAS*, 381, 41
- Hahn O., Porciani C., Carollo C. M., Dekel A., 2007, *MNRAS*, 375, 489
- Hayashi E., Navarro J. F., Springel V., 2007, *MNRAS*, 377, 50
- Helmi A., 2004, *ApJ*, 610, L97
- Hockney R. W., Eastwood J. W., 1988, *Computer simulation using particles*. Bristol: Hilger, 1988
- Hoekstra H., Yee H. K. C., Gladders M. D., 2004, *ApJ*, 606, 67
- Hopkins P. F., Bahcall N. A., Bode P., 2005, *ApJ*, 618, 1
- Ibata R., Lewis G. F., Irwin M., Totten E., Quinn T., 2001, *ApJ*, 551, 294
- Jing Y. P., Suto Y., 2002, *ApJ*, 574, 538
- Johnston K. V., Law D. R., Majewski S. R., 2005, *ApJ*, 619, 800
- Kang X., van den Bosch F. C., Yang X., Mao S., Mo H. J., Li C., Jing Y. P., 2007, *MNRAS*, 378, 1531
- Kasun S. F., Evrard A. E., 2005, *ApJ*, 629, 781
- Kazantzidis S., Kravtsov A. V., Zentner A. R., Allgood B., Nagai D., Moore B., 2004, *ApJ*, 611, L73
- Kitzbichler M. G., Saurer W., 2003, *ApJ*, 590, L9
- Knebe A., Gill S. P. D., Gibson B. K., Lewis G. F., Ibata R. A., Dopita M. A., 2004, *ApJ*, 603, 7
- Koposov S. E., Rix H.-W., Hogg D. W., 2010, *ApJ*, 712, 260
- Kuhlen M., Diemand J., Madau P., 2007, *ApJ*, 671, 1135
- Lau E. T., Nagai D., Kravtsov A. V., Zentner A. R., 2011, *ApJ*, 734, 93
- Law D. R., Johnston K. V., Majewski S. R., 2005, *ApJ*, 619, 807
- Law D. R., Majewski S. R., 2010, *ApJ*, 714, 229
- Law D. R., Majewski S. R., Johnston K. V., 2009, *ApJ*, 703, L67
- Lee J., Jing Y. P., Suto Y., 2005, *ApJ*, 632, 706
- Lemson G., Kauffmann G., 1999, *MNRAS*, 302, 111
- Libeskind N. I., Cole S., Frenk C. S., Okamoto T., Jenkins A., 2007, *MNRAS*, 374, 16
- Libeskind N. I., Frenk C. S., Cole S., Helly J. C., Jenkins A., Navarro J. F., Power C., 2005, *MNRAS*, 363, 146
- Libeskind N. I., Knebe A., Hoffman Y., Gottlöber S., Yepes G., Steinmetz M., 2011, *MNRAS*, 411, 1525
- Macciò A. V., Dutton A. A., van den Bosch F. C., Moore B., Potter D., Stadel J., 2007, *MNRAS*, 378, 55
- Martínez-Delgado D., Gómez-Flechoso M. Á., Aparicio A., Carrera R., 2004, *ApJ*, 601, 242
- Navarro J. F., Ludlow A., Springel V., Wang J., Vogelsberger M., White S. D. M., Jenkins A., Frenk C. S., Helmi A., 2010, *MNRAS*, 402, 21
- Niederste-Ostholt M., Strauss M. A., Dong F., Koester B. P., McKay T. A., 2010, *MNRAS*, 405, 2023
- Olling R. P., 1996, *AJ*, 112, 481
- Patiri S. G., Cuesta A. J., Prada F., Betancort-Rijo J., Klypin A., 2006, *ApJ*, 652, L75
- Paz D. J., Sgró M. A., Merchán M., Padilla N., 2011, *MNRAS*, pp 502–+
- Pedrosa S., Tissera P. B., Scannapieco C., 2009, *MNRAS*, 395, L57
- Pimbblet K. A., 2005, *MNRAS*, 358, 256
- Power C., Navarro J. F., Jenkins A., Frenk C. S., White S. D. M., Springel V., Stadel J., Quinn T., 2003, *MNRAS*, 338, 14
- Quinn T., Binney J., 1992, *MNRAS*, 255, 729
- Ragone-Figueroa C., Plionis M., Merchán M., Gottlöber S., Yepes G., 2010, *MNRAS*, 407, 581
- Rix H., 1996, in L. Blitz & P. J. Teuben ed., *Unsolved Problems of the Milky Way Vol. 169 of IAU Symposium, The Shapes of Dark Halos*. pp 23–29
- Robotham A., Phillipps S., De Propris R., 2008, *ApJ*, 672, 834
- Rossi G., Sheth R. K., Tormen G., 2010, preprint (ArXiv:1010.2839)
- Sackett P. D., 1999, in D. R. Merritt, M. Valluri, & J. A. Sellwood ed., *Galaxy Dynamics - A Rutgers Symposium Vol. 182 of Astronomical Society of the Pacific Conference Series, The Shape of Dark Matter Halos*. p. 393
- Sales L. V., Navarro J. F., Lambas D. G., White S. D. M., Croton D. J., 2007, *MNRAS*, 382, 1901
- Salvador-Solé E., Serra S., Manrique A., González-Casado G., 2011, preprint (ArXiv:1104.3143)
- Siebert A., Bienaymé O., Binney J., Bland-Hawthorn J., Campbell R., Freeman K. C., Gibson B. K., Gilmore G., Grebel E. K., Helmi A., Munari U., Navarro J. F., Parker Q. A., Seabroke G., Siviero A., Steinmetz M., et al. 2008, *MNRAS*, 391, 793
- Spergel D. N., Steinhardt P. J., 2000, *Physical Review Letters*, 84, 3760
- Springel V., Wang J., Vogelsberger M., Ludlow A., Jenkins A., Helmi A., Navarro J. F., Frenk C. S., White S. D. M., 2008, *MNRAS*, 391, 1685
- Springel V., White S. D. M., Hernquist L., 2004, in S. Ryder, D. Pisano, M. Walker, & K. Freeman ed., *Dark Matter in Galaxies Vol. 220 of IAU Symposium, The shapes of simulated dark matter halos*. p. 421
- Springel V., White S. D. M., Tormen G., Kauffmann G., 2001, *MNRAS*, 328, 726
- Stadel J., Potter D., Moore B., Diemand J., Madau P., Zemp M., Kuhlen M., Quilis V., 2009, *MNRAS*, 398, L21
- Stoica R. S., Martínez V. J., Mateu J., Saar E., 2005, *A&A*, 434, 423
- Strigari L. E., Kaplinghat M., Bullock J. S., 2007, *Phys. Rev. D*, 75, 061303
- Swaters R. A., Sancisi R., van der Hulst J. M., 1997, *ApJ*, 491, 140
- Thomas P. A., Colberg J. M., Couchman H. M. P., Efstathiou G. P., Frenk C. S., Jenkins A. R., Nelson A. H., Hutchings R. M., Peacock J. A., Pearce F. R., White S. D. M., 1998, *MNRAS*, 296, 1061
- Tissera P. B., White S. D. M., Pedrosa S., Scannapieco C., 2010, *MNRAS*, 406, 922
- Tormen G., 1997, *MNRAS*, 290, 411
- Toth G., Ostriker J. P., 1992, *ApJ*, 389, 5
- Valluri M., Debattista V. P., Quinn T., Moore B., 2010, *MNRAS*, 403, 525
- Vogelsberger M., White S. D. M., 2011, *MNRAS*, 413, 1419
- Vogelsberger M., White S. D. M., Mohayaee R., Springel V., 2009, *MNRAS*, 400, 2174
- Wang J., White S. D. M., 2009, *MNRAS*, 396, 709
- Warnick K., Knebe A., Power C., 2008, *MNRAS*, 385, 1859
- Warren M. S., Quinn P. J., Salmon J. K., Zurek W. H., 1992, *ApJ*, 399, 405
- Yang X., van den Bosch F. C., Mo H. J., Mao S., Kang X., Weinmann S. M., Guo Y., Jing Y. P., 2006, *MNRAS*, 369,

1293

Yoshida N., Springel V., White S. D. M., Tormen G., 2000, ApJ, 544, L87

Zhang Y., Yang X., Faltenbacher A., Springel V., Lin W., Wang H., 2009, ApJ, 706, 747

## APPENDIX A: THE SHAPE OF DARK MATTER HALOES: METHODS

In this section we provide a review of the various methods that have been proposed in the literature to measure dark matter halo shapes and compare the results when applied to the same object. The methods most commonly used are the diagonalization of the inertia tensor and the characterization with ellipsoids of either the interpolated density field or the underlying gravitational potential (Warnick et al. 2008). We introduce as well an additional scheme, which incorporates the advantages of different pre-existing methods, and where halo shapes are determined by fitting ellipsoids to the 3D iso-density surfaces.

### A1 Inertia tensor

One of the drawbacks of methods based on the determination of the inertia tensor is its quadratic relation with distance, which assigns the largest weight to particles residing far away from the centre, an issue complicated further by the presence of substructures in the outskirts of the dark matter haloes.

The bias introduced by this distance weighting can be alleviated by normalizing each coordinate with some measure of distance (Gerhard 1983; Dubinski & Carlberg 1991). In this case the “reduced” inertia tensor

$$I_{ij} = \sum_{\mathbf{x}_k \in V} \frac{x_k^{(i)} x_k^{(j)}}{d_k^2}, \quad (\text{A1})$$

where  $d_k$  is a distance measure to the  $k$ -th particle and  $V$  is a set of particles’ positions. Assuming that dark matter haloes can be represented by ellipsoids, the axis ratios are the ratios of the square-roots of the eigenvalues of  $\mathbf{I}$ , and the directions of the principal axes are given by the corresponding eigenvectors. To determine the axis lengths (e.g.  $b$  and  $c$ ) however requires knowledge of the third axis ( $a$ ). Therefore there are different choices to be made in this method, namely, which is the initial set of points  $V$ , the distance measure  $d$  and the way in which  $a$  is defined. Different approaches have been followed to set these quantities.

- Warren et al. (1992) use an iterative scheme keeping the ellipsoid volume constant. The set  $V$ , initially chosen to be a spherical shell, is iteratively deformed and reoriented using the eigenvalues and eigenvectors of the reduced inertia tensor. These authors take  $d$  to be the Euclidean distance to a given particle. Bailin & Steinmetz (2005), however, argue that this systematically overpredicts the roundness of the haloes. In the figures below we have modified Warren et al.’s method by using  $d_k^2 = x_k^2 + y_k^2/q^2 + z_k^2/s^2$  instead, and where  $q = b/a$  and  $s = c/a$  are updated in each iteration. We define also the shell’s radii using this definition of distance, instead of the Euclidean one.

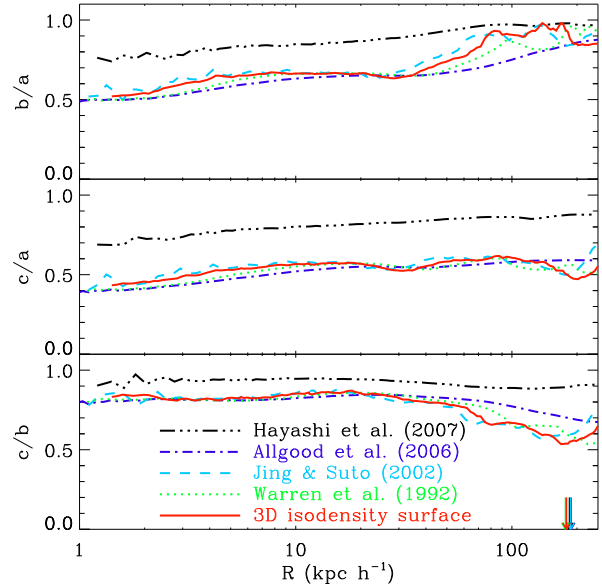


**Figure A2.** Axis ratios ( $a \geq b \geq c$ ) for Aq-A-4 as a function of the ellipsoidal distance  $R = (abc)^{1/3}$ . The solid red line corresponds to our new algorithm, while dot-dashed black, dashed cyan, dot-dashed blue and dotted green correspond respectively, to: iso-potential contours (Hayashi et al. 2007), particle-based isodensity inertia tensor (Jing & Suto 2002), normalized inertia tensor diagonalized upon hollow (Warren et al. 1992) and on solid (Allgood et al. 2006) ellipsoids. Vertical arrows indicate the size of the virial ellipsoid,  $R_{\text{vir}}$ , for each method. All methods agree well, especially in the inner regions ( $R \lesssim 100h^{-1}$  kpc).

- Allgood et al. (2006) also employ an iterative scheme but now keeping the largest axis length constant. Initially the set  $V$  is selected to be given by all particles located inside a sphere (as opposed to a spherical shell of a given radius) which is reshaped iteratively using the eigenvalues. As before, the orientation is determined from the eigenvectors of  $\mathbf{I}$ , and the distance measure used is  $d_k^2 = x_k^2 + y_k^2/q^2 + z_k^2/s^2$ . In the figures below we have removed all bound substructures contained in a halo. This alleviates the noise and artificial tilting of the ellipsoids that is introduced by such substructures. We use SUBFIND (Springel et al. 2001) to identify and remove particles associated to subhaloes within the region of interest.

In our implementations the iterations are stopped when convergence in the axis ratios is reached, which we take to be when the relative change is smaller than  $10^{-6}$ , or when  $V$  is composed by less than 3000 particles. If the latter condition is not fulfilled the shape of such a contour is not considered in our analysis.

### A2 Density

An alternative approach to determine halo shapes is to consider the underlying density field, which carries more information about the internal mass distribution of the haloes than the inertia tensor. We explore here two different implementations.

- Jing & Suto (2002) determine the shape by fitting ellipsoids to sets of particles having (nearly) the same nearest



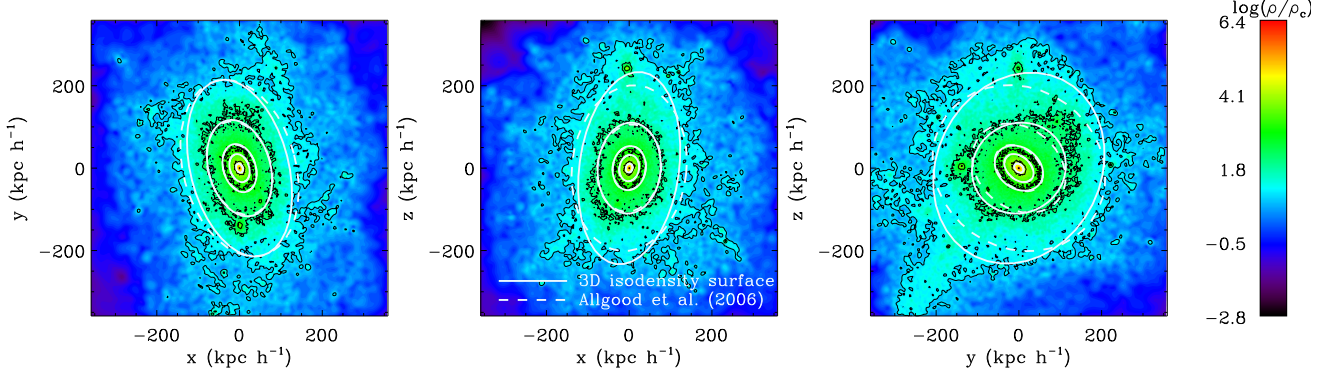


**Figure A1.** Dark matter density in thin slices centred on the  $z = 0$  (left)  $y = 0$  (centre) and  $x = 0$  (right) planes. The black lines represent the isodensity contours. The solid white ellipses correspond to our new density-based method, while the dashed ones are for the inertia tensor method described by Allgood et al. (2006). In the inner regions both methods agree very well and follow the isodensity surface, however closer to the virial radius (the external most contour) the inertia tensor-based scheme predicts somewhat rounder shapes than the actual density distribution.

neighbours-based density. Noise due to substructures is effectively removed by an implementation of the Friends of Friends (FOF) algorithm to these sets (Davis et al. 1985), and where the linking length is selected to vary from set to set of iso-density particles according to the empirical law  $l = 3(\rho/m)^{-1/3}$ .

- We present a new method based on fitting an ellipsoid to the particle density. We first create a continuous density field out of the particles positions. We do so by using a Cloud-In-Cell algorithm that allows the reconstruction of the density field on a regular grid (Hockney & Eastwood 1988). For better resolution and to keep the computational cost relatively low, the region covered by the grid is iteratively increased. The second step involves the identification of iso-density contours. We select the cells with nearly the same density and a version of the FOF algorithm is used to get rid of cells associated to substructures artificially linked to the main contour. Finally, we minimize the function:

$$S(\mathbf{M}) = \frac{1}{n} \sum_{k=1}^n \left( 1 - \sqrt{\mathbf{x}_k^T \mathbf{M} \mathbf{x}_k} \right)^2, \quad (\text{A2})$$

with  $\mathbf{M}$  the matrix representation of an ellipsoid, in order to determine the axis lengths (eigenvalues of  $\mathbf{M}$ ) and directions (eigenvectors). Notice that the minimization is carried out in a 6 dimensional space ( $\mathbf{M}$  has just 6 independent elements), therefore an educated initial guess for the iteration may reduce the numerical effort. We provide this guess by diagonalizing the inertia tensor of the cells with similar values of the density.

Fig. A1 shows 2D slices of the density map computed for halo Aq-A-4, together with several best-fit ellipsoids found by the method just outlined. An important feature of our method is that all the information about the 3D isodensity surface is taken into account; this is particularly useful towards the outskirts of the dark matter haloes where, as can be appreciated from Fig. A1, density contours become less symmetric. For comparison, we also show the results of applying the algorithm by Allgood et al. (2006) (after subhaloes subtraction) in dashed lines. Recall that in our new method ellipsoids are effectively independent of each

other and therefore this method is more sensitive to local variations of the halo shapes. On the other hand, Allgood et al. (2006) use the whole set of particles within a given radius, which implies that the shape of a contour at a given distance is correlated with the shape at smaller radii, as a careful inspection of this figure shows.

### A3 Potential

A viable alternative to the density-based methods to measure the shape of a dark matter halo is to use the gravitational potential field defined by the particles. As first noticed by Springel et al. (2004) and later confirmed by Hayashi et al. (2007), substructures cause significant fluctuations in the local density distribution, but their contribution to the gravitational potential is considerably less harmful (Springel et al. 2004; Hayashi et al. 2007). Iso-potential contours are therefore smoother and more regular than those defined by the density field. Taking advantage of this feature, Hayashi et al. (2007) have implemented a method to characterize the structural shape of dark matter haloes by fitting ellipses to the iso-potential contours computed on three orthogonal 2D planes. It is important to note here that the potential is intrinsically rounder than the density distribution, for example for a cored logarithmic potential  $1 - (c/a)_\rho \approx 3[1 - (c/a)_\Phi]$  outside the core (Binney & Tremaine 2008).

### A4 Results

In Fig. A2, we compare the shape as a function of the ellipsoidal radius obtained for the halo Aq-A-4 using the methods described above. This figure shows very good agreement in the halo shapes measured by the different methods, especially in the inner regions ( $R \lesssim 100h^{-1}$  kpc). There is however an indication that at large radii, density-based methods (red solid and light-blue dashed curves) tend to give slightly more oblate shapes (higher  $b/a$ ) than those based on implementations of the inertia tensor, but the effect is only marginal. As expected, the method based on the gravita-

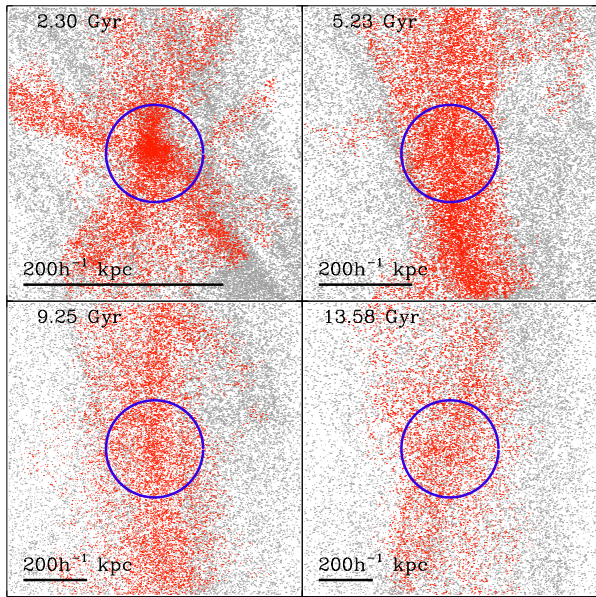


**Figure B1.** Distribution of particles around Aq-A halo at four different times. Particles with a single caustic crossing are plotted in red and are seen to trace reasonably well the filamentary structure surrounding the halo. Each box has been rotated according to the inertia tensor defined by this subset of particles.

tional potential (Hayashi et al. 2007) produces higher axis ratios (blue dotted line).

## APPENDIX B: THE SIZE OF FILAMENTS AT DIFFERENT TIMES

Dark matter haloes that reside in a filament will acquire their mass preferentially along the filament’s longest axis. As discussed in Sec. 5, such infall of material gives rise to a power spectrum characterized by a significant  $l = 2$  component. However, when the surrounding filament is sufficiently wide, i.e. of comparable or larger cross-section than the virial radius of the halo, the infalling particles will appear to be more isotropically distributed on the sky, shifting the power to the  $l = 0$  term of the spectrum. We have argued in Section 5 of this paper that the latter case is characteristic of the late stages of mass assembly in  $\sim 10^{12} M_\odot$  objects. We analyze this statement in more detail in this Appendix, and provide a suitable measurement of a filament’s size and compare it to that of the dark matter halo it hosts. For brevity we focus our analysis on halo Aq-A, but our conclusions should hold in the general case.

The measurement of the size of a filament is not completely straightforward and may depend on the particular algorithm used for its identification (Stoica et al. 2005; Zhang et al. 2009). In this work we define structures according to the number of caustic crossings of its constituent particles. Caustics arise during the gravitational collapse of a dynamical system. In the case of cold dark matter, the initial velocities of particles are negligible, and thus these are distributed in 3D sheets in phase-space (Bertschinger 1985). Their collapse and subsequent virialization may be seen as the folding of these sheets, and the location of these folds in configuration space gives rise to caustics. Therefore the number of

caustic crossings is indicative of the degree of virialization of a dynamical system.

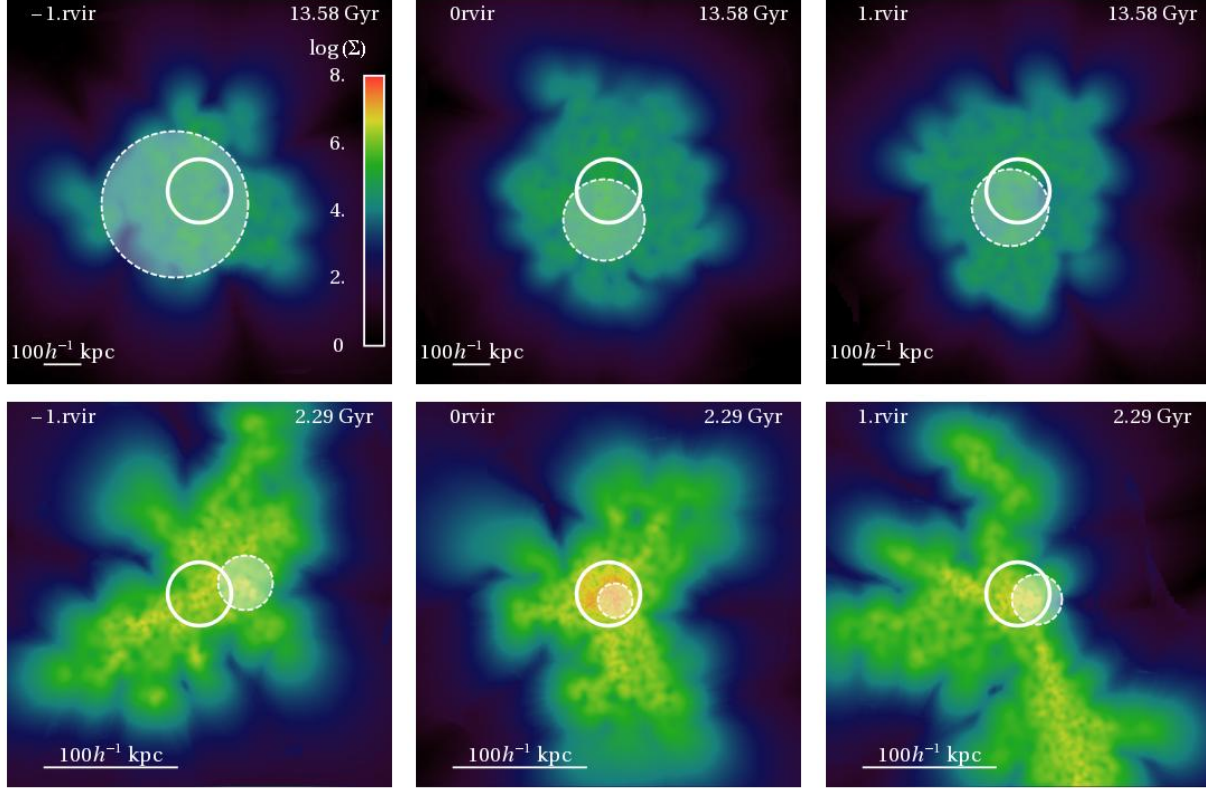
For example particles with zero crossings remain under the quasi-linear regime and have therefore not collapsed into any virialized structure today. As gravitational collapse proceeds, the number of caustics that a particle experiences increases rapidly. As shown in Vogelsberger & White (2011, Fig. 4), particles with 1 or 2 caustic crossings delineate the surrounding filamentary structure of a halo, whereas those with a higher number of crossings belong to the host halo itself. Therefore, in this work we select particles with 1 caustic crossing to study the properties of the filamentary structure surrounding Aq-A halo at different epochs (Vogelsberger et al. 2009; Vogelsberger & White 2011).

Fig. B1 shows the distribution of particles in a box of size  $6r_{\text{vir}}$  at four different times, where those with a single caustic crossing are highlighted in red. The circle indicates the corresponding virial radius of the Aq-A halo, and the horizontal bar gives the reference for conversion to the physical scale. At each time-step we have rotated the reference frame to the principal axis of the inertia tensor defined by the particles with 1 caustic crossing<sup>4</sup>. This figure shows these particles successfully trace the filamentary structure around this halo. Interestingly, there is a hint of evolution in the relative size of the filament with respect to that of the halo: as we move back in time, the red particles change from fully encompassing the halo ( $t \geq 9$  Gyr) to having a similar cross-section ( $t \sim 5.25$  Gyr) to becoming even narrower at earlier times ( $t \sim 2.3$  Gyr). At this point the geometry of the system is much more complex due to multiple filaments feeding material to the central object.

In order to quantify the evolution in the cross section of a filament we proceed as follows. We rotate the reference system such that the  $z$ -direction is that given by the inertia tensor of particles with 1 caustic crossing. We identify planes perpendicular to this direction and label the positions of such planes as  $z_p$ , where  $z_p = [-2, -1.5, -1, \dots, +1.5, +2] r_{\text{vir}}$ . We project in each plane all selected particles that satisfy  $|z_i - z_p| \leq 0.5 r_{\text{vir}}$ . We compute the (projected) density of neighbours of each particle in the plane using a 2D SPH kernel and identify the particle with the highest density. This particle’s location sets the centroid of the filament and its density at the core. We then define the radius of the filament  $r_{\text{fil}}$  as the distance from this centroid where the density has dropped to 60% of its central value. Although this definition is arbitrary, this allows a measurement of the relative size at different times.

Fig. B2 illustrates our procedure for two different times:  $t = 13.6$  (top) and  $t = 2.3$  (bottom) Gyr; applied to 3 different planes along the  $z$ -direction:  $z_p = -r_{\text{vir}}, 0, +r_{\text{vir}}$ . Each panel shows the projected density of particles belonging to the filamentary structure (one single caustic crossing), where the virial radius of the central halo is indicated with a white (empty) circle, and the highlighted full disc indicates the size of the filament centred on the highest density point as de-

<sup>4</sup> Because we are interested in the set of filaments connected to the central object, we run a FOF algorithm over the particles with 1 caustic crossing, using a linking length of 0.7 the mean inter-particle separation and retain for the analysis only those set of particles belonging to the most massive FOF group



**Figure B2.** Projected mass density (in units of  $hM_{\odot}\text{kpc}^{-2}$ ) for three different perpendicular planes located along the direction of the filament at positions  $z_p = [-1, 0, 1]r_{\text{vir}}$ , and at two different times:  $t = 13.6$  Gyr (top) and  $t = 2.3$  Gyr (bottom). The solid white curve indicates the half the virial radius of the halo at each time and the highlighted filled disc shows the size assigned to the filament and centred in the highest density point as described in the text. The geometry of the filaments is complicated, but their relative size with respect to that of the halo is clearly larger at present day ( $t \sim 13.6$  Gyr) than it was at  $t \sim 2.3$  Gyr.

scribed above. Fig. B2 suggests that filaments are not really straight in space (as indicated by the different positions of the centroids for panels located at different  $z_p$ ) and also their geometry is complex since panels located symmetrically with respect to the centre of the halo yield significantly different sizes (e.g. top row,  $-r_{\text{vir}}$ ,  $+r_{\text{vir}}$  panels). However, there is still a clear trend indicating that the filament's relative size was smaller at early times than at the present day.

This trend is more clearly seen in Fig. B3, where we show the average size of the filament (normalized to a fraction of the instantaneous virial radius) measured as the average over 9 equally distant planes located from  $[-2r_{\text{vir}}, +2r_{\text{vir}}]$  as a function of time. The shaded region shows the scatter between the sizes derived for each of the individual planes at a fixed time. Notice that the relative filament-to-halo size at present day is almost twice as large than its value at  $t \sim 2$  Gyr. This provides further support to our observation that the infall of particles at later times results from an increased size of the filament with respect to that of the halo.

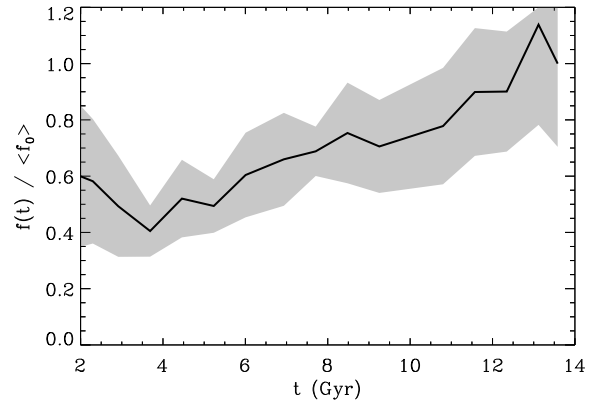


**Figure B3.** Filament size relative to the virial radius  $f = r_{\text{fil}}/(0.5r_{\text{vir}})$  as a function of time. The solid black line is the average size of the filament measured on 9 planes perpendicular to the direction of the filament. The shaded region is  $1\sigma$  scatter (see text for details). The vertical axis has been normalized to its final value at redshift zero  $f_0 = f(z=0)$  for an easier comparison.